Available online at www.sciencedirect.com
ScienceDirect
Journal of Computational Physics 227 (2008) 7294–7321
JOURNAL OF COMPUTATIONAL PHYSICS
www.elsevier.com/locate/jcp

Development of nonlinear weighted compact schemes with increasingly higher order accuracy

Shuhai Zhang [a,1], Shufen Jiang [a], Chi-Wang Shu [b,*,2]

[a] China Aerodynamics Research and Development Center, Mianyang, Sichuan 621000, China
[b] Division of Applied Mathematics, Brown University, Providence, RI 02912, USA

Received 24 December 2007; received in revised form 12 April 2008; accepted 14 April 2008
Available online 25 April 2008

Abstract

In this paper, we design a class of high order accurate nonlinear weighted compact schemes that are higher order extensions of the nonlinear weighted compact schemes proposed by Deng and Zhang [X. Deng, H. Zhang, Developing high-order weighted compact nonlinear schemes, J. Comput. Phys. 165 (2000) 22–44] and the weighted essentially non-oscillatory schemes of Jiang and Shu [G.-S. Jiang, C.-W. Shu, Efficient implementation of weighted ENO schemes, J. Comput. Phys. 126 (1996) 202–228] and Balsara and Shu [D.S. Balsara, C.-W. Shu, Monotonicity preserving weighted essentially non-oscillatory schemes with increasingly high order of accuracy, J. Comput. Phys. 160 (2000) 405–452]. These nonlinear weighted compact schemes are proposed based on the cell-centered compact scheme of Lele [S.K. Lele, Compact finite difference schemes with spectral-like resolution, J. Comput. Phys. 103 (1992) 16–42]. Instead of performing the nonlinear interpolation on the conservative variables as in Deng and Zhang (2000), we propose to directly interpolate the flux on its stencil. Using the Lax–Friedrichs flux splitting and characteristic-wise projection, the resulted interpolation formulae are similar to those of the regular WENO schemes. Hence, the detailed analysis and even many pieces of the code can be directly copied from those of the regular WENO schemes. Through systematic test and comparison with the regular WENO schemes, we observe that the nonlinear weighted compact schemes have the same ability to capture strong discontinuities, while the resolution of short waves is improved and numerical dissipation is reduced.

Keywords: Compact scheme; Weighted interpolation; WENO scheme; Smoothness indicator

1. Introduction

There are two typical approaches to design high order finite difference schemes for solving partial differential equations. The first is the traditional concept that the derivative of a function on the numerical grid is

* Corresponding author. Tel.: +1 401 863 2549; fax: +1 401 863 1355.
E-mail addresses: zhang_shuhai@tom.com (S. Zhang), shu@dam.brown.edu (C.-W. Shu).
[1] Research supported by the Chinese National Natural Science Foundation Grants 10572146 and 10772193.
[2] Research partially supported by NSF Grants DMS-0510345 and AST-0506734.

0021-9991/$ - see front matter © 2008 Elsevier Inc. All rights reserved.
doi:10.1016/j.jcp.2008.04.012

approximated by a linear combination of the function on a subset of the grid (stencil). The linear combination coefficients should satisfy certain order conditions in order to achieve a high order accurate approximation to the derivative. This is the standard finite difference method that is called a non-compact finite difference scheme by Adams and Shariff [1]. The second approach to design finite difference schemes, corresponding to the so-called compact schemes, is to form a linear combination of the unknown approximations to the derivative at the grid points in a stencil, and equate it with another linear combination of the function itself at the grid points in the same stencil. The word "compact" corresponds to the fact that for the same order of accuracy, the stencil can be more compact in the second approach. However, a linear system must be solved to obtain approximations to the derivative at the grid points for compact schemes, thus the effective stencil for the approximation of the derivative at a grid point, in terms of the function values in the mesh, is not compact at all. The most influential reference for compact schemes is [26].

The weighted essentially non-oscillatory (WENO) finite difference scheme [19] is a typical high order non-compact finite difference scheme suitable for solving convection dominated partial differential equations containing possible discontinuities in the solutions, such as the Euler or Navier–Stokes equations in computational fluid dynamics. It is an extension of the essentially non-oscillatory (ENO) scheme which was introduced by Harten et al. [15]. The accuracy can be improved to the optimal order in smooth regions while the essentially non-oscillatory property near discontinuities is maintained. The WENO idea was first introduced by Liu et al. [27], in which the authors used a cell average approach (finite volume framework) to convert an rth order ENO scheme to an $(r+1)$th order WENO scheme. Based on the pointwise finite difference ENO scheme [38,39] and by a careful design of the smoothness indicator and nonlinear weights, the WENO scheme in [19] can achieve the optimal $(2r-1)$th order accuracy when converting an rth order ENO scheme, while still keeping the essentially non-oscillatory property near shock waves. The WENO schemes have the two desirable properties that they capture discontinuities and maintain high order accuracy. It has been applied to many problems containing discontinuous solutions. We refer to the recent review paper [37] for more details.

Even though the order of accuracy for explicit finite difference WENO schemes can be designed to be arbitrarily high, such as the eleventh order WENO scheme developed by Balsara and Shu [2], the resolution of short waves of such high order explicit finite difference schemes is not ideal. The order of accuracy refers to the asymptotic behavior of the scheme for solving smooth solutions when the mesh size becomes small. In applications, for example in wave dominated problems such as aeroacoustics and turbulence, we often need to approximate solutions on a relatively coarse mesh with respect to the wave frequencies that we would like to resolve. The scheme's ability to resolve short wavelengths relative to a given mesh can be represented by a dispersion relation. The best method to simulate wave dominated problems is the spectral method [4,11,22], which is high order accurate and has the best dispersion relation. However, the spectral method has its own limitation as it imposes significant restrictions on the geometry and boundary conditions. Typical explicit high order finite difference schemes, corresponding to the choice of linear combination coefficients to maximize the order of accuracy for a given stencil, do not have optimal dispersion relations. To overcome this drawback, there are efforts in the literature to modify the linear combination coefficients in a finite difference scheme to improve its dispersion relation, at the price of lowering the achievable order of accuracy corresponding to a given stencil. Tam and Webb [42] used this strategy to develop a dispersion relation preserving (DRP) finite difference scheme. Ponziani et al. [33] and Wang and Chen [43] also used this strategy to develop optimal WENO schemes for dispersion relationships.

A good choice to simulate wave dominated problems is the compact scheme, which typically has better dispersion relation than a finite difference scheme of the same order of accuracy. Early discussion of compact schemes can be found in [17,23]. In [26], Lele developed a family of compact schemes for the first and second derivatives. Through systematic Fourier analysis, it is shown that these compact schemes have spectral-like resolution for short waves. In practice, compact approximations on a cell-centered mesh has superiority due to their smaller numerical viscosity. Nagarajan et. al [31] and Boersma [3] used staggered mesh compact schemes to simulate compressible flows. Numerical tests indicate that their methods are quite robust. Through coupling the second derivatives, Mahesh [28] developed a family of compact schemes with good spectral-like resolution. Shukla and Zhong [40] developed a compact scheme for non-uniform meshes. Upwind compact schemes were also developed [6,10,48] for solving nonlinear hyperbolic problems. The compact schemes have

been extensively applied to direct numerical simulation (DNS) and large-eddy simulation (LES) of turbulence [7,25,29,30].

Compact schemes also have their drawbacks. They usually have low or even non-existent numerical dissipation. This is an advantage for the resolution of waves, but it also causes problems for nonlinear hyperbolic problems with shock waves or sharp gradients in the solution. Supersonic turbulence boundary or mixing layers are practical examples. For this kind of problems, a natural choice is to use a hybrid scheme. In the smooth region, a compact scheme is used; while in the region near the discontinuities, a scheme that can capture shock waves without oscillations is used. There have been many efforts to test this idea. Adams and Sheriff [1] applied a hybrid compact-ENO scheme to shock turbulence interaction. Pirozzoli [32] tested a hybrid compact-WENO scheme to the same problem. Mahesh et al. [29] used a sixth order ENO scheme to compute the spatial derivatives around the shock wave in the streamwise direction (normal-shock) and a compact scheme to compute all other spatial derivatives. Although hybrid schemes can overcome some drawbacks of both numerical schemes, new problems could arise. For example, the use of a hybrid compact-ENO or compact-WENO scheme needs indicators to distinguish discontinuities. To find a suitable indicator for discontinuities in a complex flow is a difficult problem. Switching frequently between two different schemes may cause a loss in the accuracy and resolution. Moreover, because the two different schemes have quite different structures, the hybrid scheme is often not efficient in parallel computing.

Based on the cell-centered compact scheme of Lele [26], Deng and Maekawa [8] and Deng and Zhang [9] developed a class of nonlinear compact schemes based on the idea of ENO and WENO respectively. In this scheme, the flux at the cell center is computed through a nonlinear combination of several lower order formulae on the substencil similar to the numerical flux of the WENO scheme. Their numerical results indicate that, comparing with the regular ENO and WENO schemes, their nonlinear compact scheme has better wave resolution and similar ability to capture strong shock waves. Based on the Padé type compact scheme of Lele [26], Jiang et al. [21] developed a weighted compact scheme. This weighted compact scheme is a combination of several compact schemes constructed on different substencils.

In this paper, we further explore the nonlinear weighted compact scheme of Deng and Zhang [9], with the objective of improving its accuracy, performance and efficiency. First, instead of using the nonlinear interpolation of the conservative variables as in [9], we propose to directly interpolate the flux on its stencil. Using the Lax–Friedrichs flux splitting and characteristic-wise projection, the resulted interpolation formulae are similar to those of the regular WENO schemes [19]. Hence, the detailed analysis and even many pieces of the code can be directly copied from those of the regular WENO schemes. Second, we extend the weighted compact scheme to higher order accuracy, up to eighth order. Systematic numerical test and comparison are performed.

This paper is organized as follows. In Section 2, we derive the formulae for the nonlinear weighted compact schemes. Section 3 contains a Fourier analysis to systemically analyze the wave resolution of central compact and weighted compact schemes. Accuracy tests are performed in Section 4. Numerical tests for problems including strong shock waves are shown in Section 5. The convergence to steady state solutions is studied for the fourth order weighted compact scheme in Section 6. Section 7 contains concluding remarks.

2. Scheme formulation

We consider numerical approximations to the solution of the conservation law

$$\frac{\partial u}{\partial t}+\frac{\partial f(u)}{\partial x}=0. \tag{2.1}$$

A semidiscrete finite difference scheme can be represented as

$$\left(\frac{\partial u}{\partial t}\right)_i=-f_i', \tag{2.2}$$

where f_i' is the approximation to the spatial derivative at the grid node x_i. In this section, we apply the WENO idea [19] to the linear cell-centered compact scheme proposed by Lele [26] and develop a class of weighted compact schemes similar to those in [9] that can capture discontinuities.

2.1. Cell-centered compact scheme

Lele [26] proposed a linear cell-centered compact scheme which has the following form:

$$\beta f'_{i-2} + \alpha f'_{i-1} + f'_i + \alpha f'_{i+1} + \beta f'_{i+2} = c\frac{f_{i+\frac{5}{2}} - f_{i-\frac{5}{2}}}{5\Delta x} + b\frac{f_{i+\frac{3}{2}} - f_{i-\frac{3}{2}}}{3\Delta x} + a\frac{f_{i+\frac{1}{2}} - f_{i-\frac{1}{2}}}{\Delta x}. \tag{2.3}$$

Notice that the left hand side of the compact scheme (2.3) is a linear combination of the unknown approximations to the derivative f'_j at some nodes x_j near x_i, while the right hand side is a linear combination of the function itself at half nodes (cell centers) $x_{j+\frac{1}{2}}$. The constraints on the coefficients α, β, a, b and c correspond to different orders of accuracy that can be derived by matching the Taylor series coefficients and these have been listed in Lele [26]. We list them again in Table 2.1 for later use.

If $\beta = 0$, $c = 0$, a fourth order tridiagonal compact scheme is obtained with $a = \frac{3}{8}(3 - 2\alpha)$ and $b = \frac{1}{8}(22\alpha - 1)$. The corresponding scheme is:

$$\alpha f'_{i-1} + f'_i + \alpha f'_{i+1} = b\frac{f_{i+\frac{3}{2}} - f_{i-\frac{3}{2}}}{3\Delta x} + a\frac{f_{i+\frac{1}{2}} - f_{i-\frac{1}{2}}}{\Delta x}. \tag{2.4}$$

Especially, if $\alpha = \frac{1}{22}$, the coefficient b vanishes. It results in the most compact scheme as follows:

$$\alpha f'_{i-1} + f'_i + \alpha f'_{i+1} = a\frac{f_{i+\frac{1}{2}} - f_{i-\frac{1}{2}}}{\Delta x}. \tag{2.5}$$

If $\alpha = \frac{9}{62}$, we obtain a sixth order tridiagonal scheme with the same formula as (2.4).

The cell-centered compact scheme (2.3) is originally designed for a staggered grid. It is called a staggered scheme by Nagarajan et al. [31]. A Fourier analysis indicates that the wave resolution of these cell-centered compact schemes is much better than other compact schemes of the same order of accuracy. For a non-staggered grid, the cell-centered value $f_{i+\frac{1}{2}}$ can be obtained by an interpolation from the function values on the grid nodes.

2.2. Compact interpolation

Lele [26] gave a compact formula to interpolate the value on a grid node from a staggered grid. In fact, as can be seen from Fig. 2.1, the cell-centers and nodes correspond to a shift of half a mesh size. The compact interpolation provides a compact method to transfer the values between the nodes and cell-centers. Hence, we can use it to approximate the values on cell-centers:

$$\beta\hat{f}_{i-\frac{3}{2}} + \alpha\hat{f}_{i-\frac{1}{2}} + \hat{f}_{i+\frac{1}{2}} + \alpha\hat{f}_{i+\frac{3}{2}} + \beta\hat{f}_{i+\frac{5}{2}} = \frac{c}{2}(f_{i+3} + f_{i-2}) + \frac{b}{2}(f_{i+2} + f_{i-1}) + \frac{a}{2}(f_{i+1} + f_i). \tag{2.6}$$

Table 2.1
The coefficients and truncation error of the linear cell-centered compact schemes [26]

Order	Coefficients	Truncation error
Fourth	$a = \frac{1}{8}(9 - 6\alpha - 78\beta + 16c)$ $b = \frac{1}{8}(-1 + 22\alpha + 94\beta - 24c)$	$\frac{1}{1920}(9 - 62\alpha + 1618\beta - 384c)\Delta x^4 f^{(5)}$
Sixth	$a = \frac{1}{192}(225 - 206\alpha - 254\beta)$ $b = \frac{1}{128}(-25 + 414\alpha - 114\beta)$ $c = \frac{1}{384}(9 - 62\alpha + 1618\beta)$	$\frac{1}{107520}(75 - 354\alpha + 2614\beta)\Delta x^6 f^{(7)}$
Eighth	$\beta = \frac{1}{2614}(354\alpha - 75)$ $a = \frac{1}{31368}(37950 - 39275\alpha)$ $b = \frac{1}{20912}(-3550 + 65115\alpha)$ $c = \frac{1}{62736}(-6114 + 25669\alpha)$	$\frac{1}{1686343680}(96850 - 288529\alpha)\Delta x^8 f^{(9)}$
Tenth	$\beta = \frac{9675}{577058}$, $\alpha = \frac{96850}{288529}$ $a = \frac{683425}{865587}$, $b = \frac{505175}{577058}$ $c = \frac{69049}{1731174}$	$\frac{939109}{818997645312}\Delta x^{10} f^{(11)}$

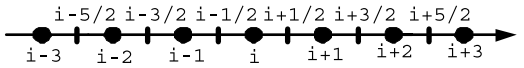

Fig. 2.1. Shift by half a mesh size between the nodes and cell-center points.

Table 2.2 lists the coefficient constraints [26] corresponding to different orders of accuracy for the compact interpolation (2.6).

2.3. Weighted interpolation

2.3.1. Basic idea of the weighted interpolation

The value on a cell center can also be interpolated locally from the node values on a stencil. In general, we can get a $(2r-1)$th order approximation based on the flux function in a stencil $S^{2r-1} = (x_{i-r+1}, \ldots, x_{i+r-1})$. Using this stencil, the flux at any point can be evaluated as a interpolating polynomial:

$$\hat{f}^{2r-1}(x) = f_i + \sum_{l=1}^{2(r-1)} a_l (x - x_i)^l. \tag{2.7}$$

Evaluating the function at the cell-center $x_{i+\frac{1}{2}}$, the $(2r-1)$th order approximation is given by:

$$\hat{f}^L_{i+\frac{1}{2}} = \hat{f}^{2r-1}(x_{i+\frac{1}{2}}) = q^{2r-1}(f_{i-r+1}, \ldots, f_{i+r-1}), \tag{2.8}$$

where the superscript L refers to the fact that the stencil S^{2r-1} is biased to the left relative to the interpolation point $x_{i+\frac{1}{2}}$, and q^{2r-1} depends linearly on the flux values f_j in the stencil S^{2r-1}.

Similar to the reconstruction in [19], the stencil S^{2r-1} can be divided into r sub-stencils

$$S^{2r-1}_k = (x_{i+k-r+1}, x_{i+k-r+2}, \ldots, x_{i+k}), \quad k = 0, 1, \ldots, r-1.$$

In each of these substencils, the rth order approximation can be obtained

$$\hat{f}^{(k)}_{i+\frac{1}{2}} = q^r_k(f_{i+k-r+1}, \ldots, f_{i+k}), \tag{2.9}$$

where

$$q^r_k(g_0, \ldots, g_{r-1}) = \sum_{l=0}^{r-1} a^r_{k,l} g_l$$

Table 2.2
Coefficients of the transfer function [26]

Order	Coefficients	Truncation error
Fourth	$a = \frac{1}{8}(9 + 10\alpha - 14\beta + 16c)$	
	$b = \frac{1}{8}(-1 + 6\alpha + 30\beta - 24c)$	$\frac{1}{128}(3 - 10\alpha + 70\beta - 128c)\Delta x^4 f^{(4)}$
Sixth	$a = \frac{1}{64}(75 + 70\alpha - 42\beta)$	
	$b = \frac{1}{128}(-25 + 126\alpha + 270\beta)$	
	$c = \frac{1}{128}(3 - 10\alpha + 70\beta)$	$\frac{1}{1024}(5 - 14\alpha + 42\beta)\Delta x^6 f^{(6)}$
Eighth	$\beta = \frac{1}{42}(14\alpha - 5)$	
	$a = \frac{1}{8}(10 + 7\alpha)$	
	$b = \frac{1}{112}(-50 + 189\alpha)$	
	$c = \frac{1}{48}(-2 + 5\alpha)$	$\frac{1}{28672}(10 - 21\alpha)\Delta x^8 f^{(8)}$
Tenth	$\beta = \frac{5}{126}$, $\alpha = \frac{10}{21}$	
	$a = \frac{5}{3}$, $b = \frac{5}{14}$	
	$c = \frac{1}{126}$	$\frac{1}{258048}\Delta x^{10} f^{(10)}$

with $a^r_{k,l}$, for $0 \leqslant k,\ l \leqslant r-1$, being constant coefficients.

The value $\hat{f}^L_{i+\frac{1}{2}}$ can be obtained by a linear combination of $\hat{f}^{(k)}_{i+\frac{1}{2}}$

$$q^{2r-1}(f_{i-r+1},\ldots,f_{i+r-1}) = \sum_{k=0}^{r-1} C^r_k q^r_k(f_{i+k-r+1},\ldots,f_{i+k}) \tag{2.10}$$

with suitable constants C^r_k, also called the linear weights.

The approximation (2.10) is linear. A scheme based on this approximation can not capture shock waves and other discontinuities without spurious oscillations. Adopting the WENO idea, we use nonlinear weights ω^r_k to replace the linear weights C^r_k and obtain a nonlinear approximation

$$\hat{f}_{i+\frac{1}{2}} = \sum_{k=0}^{r-1} \omega^r_k q^r_k(f_{i+k-r+1},\ldots,f_{i+k}), \tag{2.11}$$

where the nonlinear weight ω^r_k for the stencil S^{2r-1}_k is given by:

$$\omega^r_k = \frac{\alpha^r_k}{\alpha^r_0 + \alpha^r_1 + \cdots + \alpha^r_{r-1}} \tag{2.12}$$

with

$$\alpha^r_k = \frac{C^r_k}{(\varepsilon + IS^r_k)^2}, \quad k = 0,1,\ldots,r-1. \tag{2.13}$$

Here ε is a small positive number which is introduced to avoid the denominator becoming zero. In our later tests, we take $\varepsilon = 10^{-6}$ (except for some accuracy tests in Section 4). IS_k is the smoothness indicator of the flux function in the kth substencil which adopts the formulae given by Jiang and Shu [19] as:

$$IS^r_k = \sum_{l=1}^{r-1} \int_{x_{i-\frac{1}{2}}}^{x_{i+\frac{1}{2}}} \Delta x^{2l-1} \left(\frac{\partial^l f^{(r)}(x)}{\partial^l x}\right)^2 \mathrm{d}x. \tag{2.14}$$

2.3.2. High order nonlinear weighted approximation

In this subsection we document the explicit formulae for the high order nonlinear weighted approximations.

(*a*) For $r = 3$.In the case of $r = 3$, the linear fifth order approximation is given by

$$\hat{f}^L_{i+\frac{1}{2}} = \frac{1}{128}(3f_{i-2} - 20f_{i-1} + 90f_i + 60f_{i+1} - 5f_{i+2}). \tag{2.15}$$

The three third order approximations in the three substencils are

$$\hat{f}^0_{i+\frac{1}{2}} = \frac{1}{8}(3f_{i-2} - 10f_{i-1} + 15f_i), \tag{2.16}$$

$$\hat{f}^1_{i+\frac{1}{2}} = \frac{1}{8}(-f_{i-1} + 6f_i + 3f_{i+1}), \tag{2.17}$$

$$\hat{f}^2_{i+\frac{1}{2}} = \frac{1}{8}(3f_i + 6f_{i+1} - f_{i+2}). \tag{2.18}$$

The linear weights are given by

$$c^3_0 = \frac{1}{16}, \quad c^3_1 = \frac{10}{16}, \quad c^3_2 = \frac{5}{16}. \tag{2.19}$$

The smoothness indicators are

$$IS^3_0 = \frac{1}{4}(f_{i-2} - 4f_{i-1} + 3f_i)^2 + \frac{13}{12}(f_{i-2} - 2f_{i-1} + f_i)^2, \tag{2.20}$$

$$IS^3_1 = \frac{1}{4}(f_{i-1} - f_{i+1})^2 + \frac{13}{12}(f_{i-1} - 2f_i + f_{i+1})^2, \tag{2.21}$$

$$IS^3_2 = \frac{1}{4}(3f_i - 4f_{i+1} + f_{i+2})^2 + \frac{13}{12}(f_i - 2f_{i+1} + f_{i+2})^2. \tag{2.22}$$

The fifth order approximation in (2.15) to the cell-centered value can be written as a convex combination of the three third order approximations in (2.16)–(2.18)

$$\hat{f}^L_{i+\frac{1}{2}} = \omega_0^3 \hat{f}^0_{i+\frac{1}{2}} + \omega_1^3 \hat{f}^1_{i+\frac{1}{2}} + \omega_2^3 \hat{f}^2_{i+\frac{1}{2}}, \tag{2.23}$$

if we take the combination coefficients ω_j^3 as in (2.12).Plugging the expressions of $\hat{f}^0_{i+\frac{1}{2}}$, $\hat{f}^1_{i+\frac{1}{2}}$ and $\hat{f}^2_{i+\frac{1}{2}}$ from (2.16)–(2.18) into (2.23), we obtain

$$\begin{aligned}\hat{f}_{i+\frac{1}{2}} &= \frac{1}{16}(-f_{i-1} + 9f_i + 9f_{i+1} - f_{i+2}) + \frac{3}{8}\omega_0^3(f_{i-2} - 3f_{i-1} + 3f_i - f_{i+1}) \\ &\quad + \frac{1}{8}\left(\omega_2^3 - \frac{1}{2}\right)(f_{i-1} - 3f_i + 3f_{i+1} - f_{i+2}),\end{aligned} \tag{2.24}$$

which can be rewritten as

$$\hat{f}_{i+\frac{1}{2}} = \frac{1}{16}(-f_{i-1} + 9f_i + 9f_{i+1} - f_{i+2}) - \varphi_N(\Delta f_{i-\frac{3}{2}}, \Delta f_{i-\frac{1}{2}}, \Delta f_{i+\frac{1}{2}}, \Delta f_{i+\frac{3}{2}}), \tag{2.25}$$

where $\Delta f_{j+\frac{1}{2}} = f_{j+1} - f_j$ and

$$\varphi_N(a,b,c,d) = \frac{3}{8}\omega_0^3(a - 2b + c) + \frac{1}{8}\left(\omega_2^3 - \frac{1}{2}\right)(b - 2c + d).$$

Here, we have used the fact $\omega_0^3 + \omega_1^3 + \omega_2^3 = 1$. The formula (2.20)–(2.22) and (2.25) are similar to those for the WENO reconstruction (see (2.3) in [20]). Hence, all the analysis for the accuracy, the ability to capture strong shock waves and the convergence to steady state of the WENO schemes [16,19,44] can be copied to the weighted compact schemes discussed in this paper. For the implementation of the weighted interpolation, part of the regular WENO reconstruction code can be copied to the weighted compact schemes as well. Similar WENO interpolations have been used in [35].

(b) For $r = 4$.In the case of $r = 4$, the linear seventh order approximation is given by

$$\hat{f}^L_{i+\frac{1}{2}} = \frac{1}{1024}(-5f_{i-3} + 42f_{i-2} - 175f_{i-1} + 700f_i + 525f_{i+1} - 70f_{i+2} + 7f_{i+3}). \tag{2.26}$$

The four fourth order approximations from the four substencils are

$$\hat{f}^0_{i+\frac{1}{2}} = \frac{1}{48}(-15f_{i-3} + 63f_{i-2} - 105f_{i-1} + 105f_i), \tag{2.27}$$

$$\hat{f}^1_{i+\frac{1}{2}} = \frac{1}{48}(3f_{i-2} - 15f_{i-1} + 45f_i + 15f_{i+1}), \tag{2.28}$$

$$\hat{f}^2_{i+\frac{1}{2}} = \frac{1}{48}(-3f_{i-1} + 27f_i + 27f_{i+1} - 3f_{i+2}), \tag{2.29}$$

$$\hat{f}^3_{i+\frac{1}{2}} = \frac{1}{48}(15f_i + 45f_{i+1} - 15f_{i+2} + 3f_{i+3}). \tag{2.30}$$

The linear weights are given by

$$c_0^4 = \frac{1}{64}, \quad c_1^4 = \frac{21}{64}, \quad c_2^4 = \frac{35}{64}, \quad c_3^4 = \frac{7}{64}. \tag{2.31}$$

The smoothness indicators are

$$\begin{aligned}IS_0^4 &= f_{i-3}(79788f_{i-3} - 566568f_{i-2} + 680328f_{i-1} - 273336f_i) \\ &\quad + f_{i-2}(1027692f_{i-2} - 2523384f_{i-1} + 1034568f_i) \\ &\quad + f_{i-1}(1610892f_{i-1} - 1378728f_i) + 308748f_i^2,\end{aligned} \tag{2.32}$$

$$\begin{aligned}IS_1^4 &= f_{i-2}(38028f_{i-2} - 232488f_{i-1} + 228168f_i - 71736f_{i+1}) \\ &\quad + f_{i-1}(401292f_{i-1} - 847224f_i + 277128f_{i+1}) \\ &\quad + f_i(492012f_i - 364968f_{i+1}) + 79788f_{i+1}^2,\end{aligned} \tag{2.33}$$

$$IS_2^4 = f_{i-1}(79788f_{i-1} - 364968f_i + 277128f_{i+1} - 71736f_{i+2}) + f_i(492012f_i - 847224f_{i+1} + 228168f_{i+2}) + f_{i+1}(401292f_{i+1} - 232488f_{i+2}) + 38028f_{i+2}^2, \tag{2.34}$$

$$IS_3^4 = f_i(308748f_i - 1378728f_{i+1} + 1034568f_{i+2} - 273336f_{i+3}) + f_{i+1}(1610892f_{i+1} - 2523384f_{i+2} + 680328f_{i+3}) + f_{i+2}(1027692f_{i+2} - 566568f_{i+3}) + 79788f_{i+3}^2. \tag{2.35}$$

(c) For $r = 5$.In the case of $r = 5$, the linear ninth order approximation is given by

$$\hat{f}^L_{i+\frac{1}{2}} = \frac{1}{32768}(35f_{i-4} - 360f_{i-3} + 1764f_{i-2} - 5880f_{i-1} + 22050f_i + 17640f_{i+1} - 2940f_{i+2} + 504f_{i+3} - 45f_{i+4}). \tag{2.36}$$

The five fifth order approximations from the five substencils are

$$\hat{f}^0_{i+\frac{1}{2}} = \frac{1}{384}(105f_{i-4} - 540f_{i-3} + 1134f_{i-2} - 1260f_{i-1} + 945f_i), \tag{2.37}$$

$$\hat{f}^1_{i+\frac{1}{2}} = \frac{1}{384}(-15f_{i-3} + 84f_{i-2} - 210f_{i-1} + 420f_i + 105f_{i+1}), \tag{2.38}$$

$$\hat{f}^2_{i+\frac{1}{2}} = \frac{1}{384}(9f_{i-2} - 60f_{i-1} + 270f_i + 180f_{i+1} - 15f_{i+2}), \tag{2.39}$$

$$\hat{f}^3_{i+\frac{1}{2}} = \frac{1}{384}(-15f_{i-1} + 180f_i + 270f_{i+1} - 60f_{i+2} + 9f_{i+3}), \tag{2.40}$$

$$\hat{f}^4_{i+\frac{1}{2}} = \frac{1}{384}(105f_i + 420f_{i+1} - 210f_{i+2} + 84f_{i+3} - 15f_{i+4}). \tag{2.41}$$

The linear weights are given by

$$c_0^5 = \frac{1}{256}, \quad c_1^5 = \frac{9}{64}, \quad c_2^5 = \frac{63}{128}, \quad c_3^5 = \frac{21}{64}, \quad c_2^5 = \frac{9}{256}. \tag{2.42}$$

The smoothness indicators are

$$IS_0 = f_{i-4}(1114835f_{i-4} - 10262008f_{i-3} + 17985252f_{i-2} - 14254360f_{i-1} + 4301446f_i) + f_{i-3}(23768432f_{i-3} - 83962416f_{i-2} + 67148512f_{i-1} - 20460952f_i) + f_{i-2}(74964492f_{i-2} - 121605168f_{i-1} + 37653348f_i) + f_{i-1}(50449520f_{i-1} - 32188024f_i) + 5347091f_i^2, \tag{2.43}$$

$$IS_1 = f_{i-3}(329267f_{i-3} - 2899576f_{i-2} + 4740132f_{i-1} - 3385432f_i + 886342f_{i+1}) + f_{i-2}(6595472f_{i-2} - 22176048f_{i-1} + 16196128f_i - 4311448f_{i+1}) + f_{i-1}(19389420f_{i-1} - 29385264f_i + 8042340f_{i+1}) + f_i(11710736f_i - 6846904f_{i+1}) + 1114835f_{i+1}^2, \tag{2.44}$$

$$IS_2 = f_{i-2}(329267f_{i-2} - 2406328f_{i-1} + 3199908f_i - 1845208f_{i+1} + 393094f_{i+2}) + f_{i-1}(4914800f_{i-1} - 13983024f_i + 8404960f_{i+1} - 1845208f_{i+2}) + f_i(10783116f_i - 13983024f_{i+1} + 3199908f_{i+2}) + f_{i+1}(4914800f_{i+1} - 2406328f_{i+2}) + 329267f_{i+2}^2, \tag{2.45}$$

$$IS_3 = f_{i-1}(1114835f_{i-1} - 6846904f_i + 8042340f_{i+1} - 4311448f_{i+2} + 886342f_{i+3}) + f_i(11710736f_i - 29385264f_{i+1} + 16196128f_{i+2} - 3385432f_{i+3}) + f_{i+1}(19389420f_{i+1} - 22176048f_{i+2} + 4740132f_{i+3}) + f_{i+2}(6595472f_{i+2} - 2899576f_{i+3}) + 329267f_{i+3}^2, \tag{2.46}$$

$$\begin{aligned} IS_4 = {} & f_i(5347091f_i - 32188024f_{i+1} + 37653348f_{i+2} - 20460952f_{i+3} + 4301446f_{i+4}) \\ & + f_{i+1}(50449520f_{i+1} - 121605168f_{i+2} + 67148512f_{i+3} - 14254360f_{i+4}) \\ & + f_{i+2}(74964492f_{i+2} - 83962416f_{i+3} + 17985252f_{i+4}) \\ & + f_{i+3}(23768432f_{i+3} - 10262008f_{i+4}) + 1114835f_{i+4}^2. \end{aligned} \tag{2.47}$$

The fourth order centered compact scheme combined with the fifth order weighted interpolation results in a fourth order weighted compact scheme, to be denoted by WCOMP4 later. The sixth order centered compact scheme combined with the fifth order and the seventh order weighted interpolations results in a fifth order and a sixth order weighted compact scheme respectively, denoted by WCOMP5 and WCOMP6. The eighth order centered compact scheme combined with the seventh order and the ninth order weighted interpolations results in a seven order and an eighth order weighted compact scheme respectively, denoted by WCOMP7 and WCOMP8. Finally, the tenth order centered compact scheme combined with the ninth order weighted interpolation results in a ninth order weighted compact scheme, denoted by WCOMP9.

2.4. Boundary conditions

For non-periodic boundary conditions, the numerical scheme described in the previous sections can be used to compute the flow variables in inner points. Besides this, the numerical scheme near the boundary is also required. In this paper, we use the numerical boundary scheme proposed by Carpenter et al. [5] and Zhong [48] to compute the physical variables at free flow boundary. For fourth order accuracy, this boundary scheme is given by

$$f_0' + 3f_1' = \frac{1}{6\Delta x}(-17f_0 + 9f_1 + 9f_2 - f_3), \tag{2.48}$$

$$f_0' + 4f_1' + f_2' = \frac{1}{\Delta x}(-3f_0 + 3f_2), \tag{2.49}$$

$$f_N' + 3f_{N-1}' = \frac{1}{6\Delta x}(f_{N-3} - 9f_{N-2} - 9f_{N-1} + 17f_N), \tag{2.50}$$

$$f_N' + 4f_{N-1}' + f_{N-2}' = \frac{1}{\Delta x}(3f_N - 3f_{N-2}). \tag{2.51}$$

For solid wall boundary, through introducing ghost points, the spatial derivatives are symmetric to the wall except that of the velocity component in the direction perpendicular to the wall which is anti-symmetric.

2.5. Flux splitting

The purpose of flux splitting is to introduce correct upwinding. In general, the flux can be split into two parts:

$$f(u) = f^+(u) + f^-(u), \tag{2.52}$$

where $\frac{df^+(u)}{du} \geqslant 0$ and $\frac{df^-(u)}{du} \leqslant 0$. In this paper, we use the Lax–Friedrichs flux splitting

$$f^\pm(u) = \frac{1}{2}(f(u) \pm \alpha u), \tag{2.53}$$

where $\alpha = \max_u |f'(u)|$ with the maximum taken over some relevant range of u. For systems this α is chosen differently for each characteristic field as the maximum of the corresponding eigenvalue of the Jacobian in that field. We refer to [19] for the details of this process in the context of the WENO reconstruction which is similar to our WENO interpolation.

During the weighted interpolation for the cell-centered value, we use the upwind biased stencils to get the approximation $f_{i+\frac{1}{2}}$. That is, the value $f^+_{i+\frac{1}{2}}$ is interpolated from the point values in the stencil $S^+ = (x_{i-r+1}, \ldots, x_{i+r-1})$ and the value $f^-_{i+\frac{1}{2}}$ from $S^- = (x_{i-r+2}, \ldots, x_{i+r})$.

In this section, we just give the formulae of the fifth order interpolation as an example. $f^+_{i+\frac{1}{2}}$ is computed with Eq. (2.25) on the stencil containing the five points $i-2$, $i-1$, i, $i+1$ and $i+2$. It takes the form:

$$\hat{f}^+_{i+\frac{1}{2}} = \frac{1}{16}(-f^+_{i-1} + 9f^+_i + 9f^+_{i+1} - f^+_{i+2}) - \varphi_N(\Delta f^+_{i-\frac{3}{2}}, \Delta f^+_{i-\frac{1}{2}}, \Delta f^+_{i+\frac{1}{2}}, \Delta f^+_{i+\frac{3}{2}}). \tag{2.54}$$

Similarly, $f^-_{i+\frac{1}{2}}$ is computed on the stencil containing the five points $i-1$, i, $i+1$, $i+2$ and $i+3$. It takes the form:

$$\hat{f}^-_{i+\frac{1}{2}} = \frac{1}{16}(-f^-_{i-1} + 9f^-_i + 9f^-_{i+1} - f^-_{i+2}) + \varphi_N(\Delta f^-_{i+\frac{5}{2}}, \Delta f^-_{i+\frac{3}{2}}, \Delta f^-_{i+\frac{1}{2}}, \Delta f^-_{i-\frac{1}{2}}). \tag{2.55}$$

Adding together $f^+_{i+\frac{1}{2}}$ and $f^-_{i+\frac{1}{2}}$ gives the cell-centered value $f_{i+\frac{1}{2}}$

$$\hat{f}_{i+\frac{1}{2}} = \frac{1}{16}(-f_{i-1} + 9f_i + 9f_{i+1} - f_{i+2}) - \varphi_N(\Delta f^-_{i+\frac{5}{2}}, \Delta f^-_{i+\frac{3}{2}}, \Delta f^-_{i+\frac{1}{2}}, \Delta f^-_{i-\frac{1}{2}}) + \varphi_N(\Delta f^+_{i-\frac{3}{2}}, \Delta f^+_{i-\frac{1}{2}}, \Delta f^+_{i+\frac{1}{2}}, \Delta f^+_{i+\frac{3}{2}}). \tag{2.56}$$

2.6. Time discretization

After the spatial derivative is discretized, we obtain a set of ordinary differential equations

$$\frac{\mathrm{d}u}{\mathrm{d}t} = L(u), \tag{2.57}$$

where the operator $L(u) = -f_x$ and f_x at the grid points is approximated by the compact scheme (2.3) combined with the compact interpolation or weighted interpolation. This set of ordinary differential equations can be discretized by the third order TVD Runge–Kutta method [38] as follows:

$$u^{(1)} = u^n + \Delta t L(u^n), \tag{2.58}$$

$$u^{(2)} = \frac{3}{4}u^n + \frac{1}{4}u^{(1)} + \frac{1}{4}\Delta t L(u^{(1)}), \tag{2.59}$$

$$u^{n+1} = \frac{1}{3}u^n + \frac{2}{3}u^{(2)} + \frac{2}{3}\Delta t L(u^{(2)}). \tag{2.60}$$

3. Fourier analysis of the errors

In this section, we discuss the dispersion and dissipation of the compact schemes in this paper using Fourier analysis. A periodic grid function can be represented by its trigonometric interpolation

$$f_N(x) = \sum_{k=-N/2}^{N/2-1} \hat{f}_k \exp\left(\frac{2\pi \mathrm{i} k x}{L}\right) \tag{3.1}$$

where $\mathrm{i} = \sqrt{-1}$. Differentiating the function yields

$$f'_N(s) = \sum_{k=-N/2}^{N/2-1} \mathrm{i}\omega \hat{f}_k \exp(\mathrm{i}\omega s) \tag{3.2}$$

where $\omega = 2\pi k \Delta x / L = 2\pi k / N$ and $s = x/\Delta x$ are the scaled wave number and the scaled coordinate respectively. The exact first derivative of the function (3.1) (with respect to s) has the Fourier coefficients $\hat{f}'_k = \mathrm{i}\omega \hat{f}_k$. By comparing the first derivative obtained from the finite difference scheme and the exact Fourier coefficients, the modified wave number of a finite difference scheme can be obtained. From this process, the modified wave number for the cell-centered compact scheme of Eq. (2.3) is [26]:

$$w'(\omega) = \frac{2a\sin(\omega/2) + \frac{2b}{3}\sin(3\omega/2) + \frac{2c}{5}\sin(5\omega/2)}{1 + 2\alpha\cos(\omega) + 2\beta\cos(2\omega)} \tag{3.3}$$

and the transfer function for the compact interpolation (2.6) is given by [26]:

$$T(\omega) = \frac{a\cos(\omega/2) + b\cos(3\omega/2) + c\cos(5\omega/2)}{1 + 2\alpha\cos(\omega) + 2\beta\cos(2\omega)}. \tag{3.4}$$

Fig. 3.1 shows the modified wave number of the cell-centered compact scheme. We can observe that the cell-centered compact scheme has really spectral-like resolution. Fig. 3.2 is the modified wave number of the cell-centered compact scheme coupled with the compact interpolation. It is obvious that as the order of the compact interpolation increases, the modified wave number approaches that of the cell-centered compact scheme.

The modified wave number of the cell-centered compact scheme coupled with the weighted interpolation (using linear weights) is as follows.

For the fourth order weighted compact scheme:

$$\begin{aligned}\mathrm{Real}(w'(\omega)) = {} & \frac{1}{128(1 + 2\alpha\cos(\omega) + 2\beta\cos(2\omega))}(a(175\sin(\omega) - 28\sin(2\omega) + 3\sin(3\omega)) \\ & + \frac{b}{3}(147\sin(\omega) + 150\sin(2\omega) - 25\sin(3\omega) + 3\sin(4\omega)) + \frac{c}{5}(-25\sin(\omega) + 150\sin(2\omega) \\ & + 150\sin(3\omega) - 25\sin(4\omega) + 3\sin(5\omega))),\end{aligned} \tag{3.5}$$

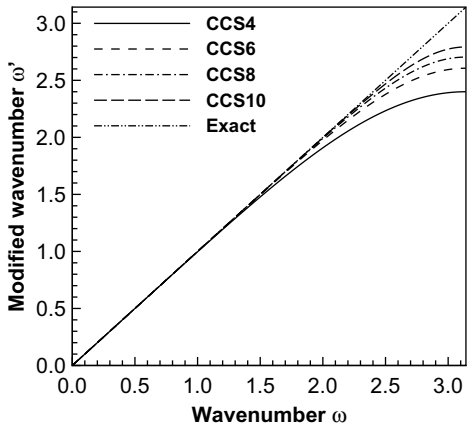

Fig. 3.1. Modified wavenumber of the cell-centered compact scheme (CCS).

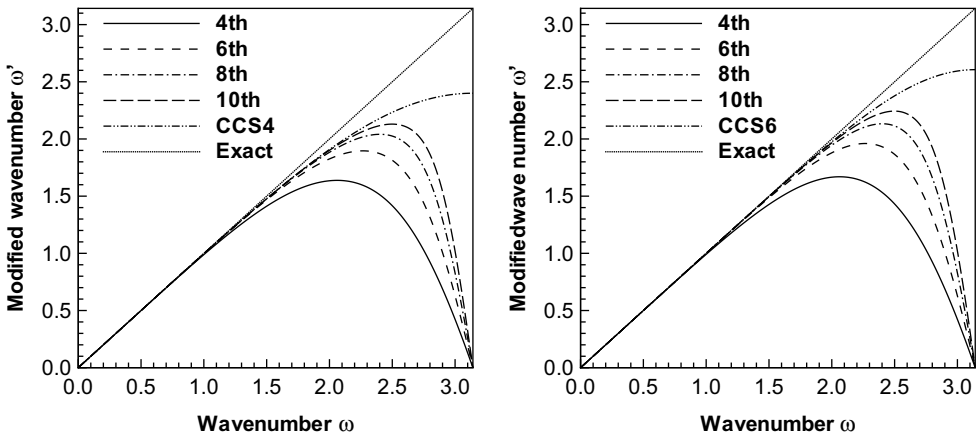

Fig. 3.2. Modified wavenumber of the cell-centered compact scheme. (left) Fourth order cell-centered compact scheme with a compact interpolation of different orders of accuracy. (right) Sixth order cell-centered compact scheme with a compact interpolation of different orders of accuracy.

$$\mathrm{Im}(w'(\omega)) = -\frac{1}{128(1+2\alpha\cos(\omega)+2\beta\cos(2\omega))}(a(30-45\cos(\omega)+18\cos(2\omega)-3\cos(3\omega)) + \frac{b}{3}(-15+33\cos(\omega)-30\cos(2\omega)+15\cos(3\omega)-3\cos(4\omega)) + \frac{c}{5}(3-15\cos(\omega)+30\cos(2\omega) - 30\cos(3\omega)+15\cos(4\omega)-3\cos(5\omega))). \quad (3.6)$$

For the sixth order weighted compact scheme:

$$\mathrm{Real}(w'(\omega)) = \frac{1}{1024(1+2\alpha\cos(\omega)+2\beta\cos(2\omega))}(a(1470\sin(\omega)-294\sin(2\omega)+54\sin(3\omega)-5\sin(4\omega)) + \frac{b}{3}(1176\sin(\omega)+1225\sin(2\omega)-245\sin(3\omega)+49\sin(4\omega)-5\sin(5\omega)) + \frac{c}{5}(-240\sin(\omega) + 1225\sin(2\omega)+1225\sin(3\omega)-245\sin(4\omega)+49\sin(5\omega)-5\sin(6\omega))), \quad (3.7)$$

$$\mathrm{Im}(w'(\omega)) = -\frac{1}{1024(1+2\alpha\cos(\omega)+2\beta\cos(2\omega))}(a(175-280\cos(\omega)+140\cos(2\omega) - 40\cos(3\omega)+5\cos(4\omega)) + \frac{b}{3}(-105+210\cos(\omega)-180\cos(2\omega)+105\cos(3\omega) - 35\cos(4\omega)+5\cos(5\omega)) + \frac{c}{5}(35-110\cos(\omega)+175\cos(2\omega)-175\cos(3\omega) + 105\cos(4\omega)-35\cos(5\omega)+5\cos(6\omega))). \quad (3.8)$$

For the eighth order weighted compact scheme:

$$\mathrm{Real}(w'(\omega)) = \frac{1}{32768(1+2\alpha\cos(\omega)+2\beta\cos(2\omega))}(a(48510\sin(\omega)-11088\sin(2\omega)+2673\sin(3\omega) - 440\sin(4\omega)+35\sin(5\omega)) + \frac{b}{3}(37422\sin(\omega)+40095\sin(2\omega)-8855\sin(3\omega) + 2268\sin(4\omega)-405\sin(5\omega)+35\sin(6\omega)) + \frac{c}{5}(-8415\sin(\omega)+39655\sin(2\omega) + 39690\sin(3\omega)-8820\sin(4\omega)+2268\sin(5\omega)-405sin(6\omega)+35\sin(7\omega))), \quad (3.9)$$

$$\mathrm{Im}(w'(\omega)) = -\frac{1}{32768(1+2\alpha\cos(\omega)+2\beta\cos(2\omega))}(a(4410-7350\cos(\omega)+4200\cos(2\omega)-1575\cos(3\omega) + 350\cos(4\omega)-35\cos(5\omega)) + \frac{b}{3}(-2940+5670\cos(\omega)-4725\cos(2\omega)+2975\cos(3\omega) - 1260\cos(4\omega)+315\cos(5\omega)-35\cos(6\omega)) + \frac{c}{5}(1260-3255\cos(\omega)+4445\cos(2\omega) - 4410\cos(3\omega)+2940\cos(4\omega)-1260\cos(5\omega)+315\cos(6\omega)-35\cos(7\omega))). \quad (3.10)$$

On the other hand, the fifth order WENO scheme [19] (using linear weights) has the modified wave number

$$\mathrm{Real}(w'(\omega)) = \frac{3}{2}\sin(\omega) - \frac{3}{10}\sin(2\omega) + \frac{1}{30}\sin(3\omega), \quad (3.11)$$

$$\mathrm{Im}(w'(\omega)) = -\frac{1}{3} + \frac{1}{2}\cos(\omega) - \frac{1}{5}\cos(2\omega) + \frac{1}{30}\cos(3\omega). \quad (3.12)$$

The seventh order WENO scheme [2] has the modified wave number

$$\mathrm{Real}(w'(\omega)) = \frac{1}{420}(672\sin(\omega)-168\sin(2\omega)+32\sin(3\omega)-3\sin(4\omega)), \quad (3.13)$$

$$\mathrm{Im}(w'(\omega)) = \frac{1}{420}(105-168\cos(\omega)+84\cos(2\omega)-24\cos(3\omega)+3\cos(4\omega)). \quad (3.14)$$

The ninth order WENO scheme [2] has the modified wave number

$$\mathrm{Real}(w'(\omega)) = \frac{1}{2520}(4200\sin(\omega) - 1200\sin(2\omega) + 300\sin(3\omega) - 50\sin(4\omega) + 4\sin(5\omega)), \tag{3.15}$$

$$\mathrm{Im}(w'(\omega)) = \frac{1}{2520}(504 - 840\cos(\omega) + 480\cos(2\omega) - 180\cos(3\omega) + 40\cos(4\omega) - 4\cos(5\omega)). \tag{3.16}$$

The real part corresponds to the dispersion term of the scheme's resolution to short waves and is shown in Fig. 3.3. The imaginary part corresponds to the dissipation and is shown in Fig. 3.4. We can see that the fourth order weighted compact scheme has almost the same resolution as that of the fifth order WENO scheme. The sixth and eighth order weighted compact schemes have better resolution to short waves than the counterparts of WENO schemes. The compact schemes have lower dissipation than the counterparts of WENO schemes.

4. Accuracy tests

In this section, we test the accuracy of the weighted compact schemes. In the following examples, we have adjusted the time step to $\Delta t = \Delta x^{\frac{r}{3}}$ for the rth order schemes so that time discretization error will not dominate.

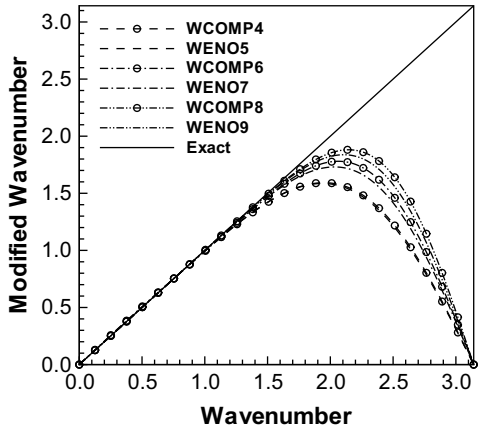

Fig. 3.3. Modified wave number of weighted compact schemes and a comparison with WENO schemes.

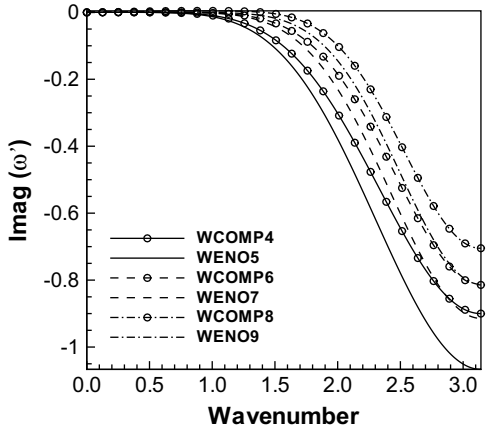

Fig. 3.4. Dissipation of the weighted compact schemes and a comparison with WENO schemes.

4.1. The accuracy of weighted compact schemes with $\varepsilon = 10^{-6}$

The parameter ε in (2.13) is a small positive number to avoid the denominator becoming zero. In most applications of WENO schemes, e.g. those in [45,46], it is taken as $\varepsilon = 10^{-6}$. We will test the accuracy with this choice of ε in this subsection.

We solve the following linear scalar equation:

$$\begin{aligned} &u_t + u_x = 0, \quad -1 \leqslant x \leqslant 1, \\ &u(x,0) = u^0(x), \quad \text{periodic} \end{aligned} \tag{4.1}$$

with three different initial conditions: $u^0(x) = \sin(\pi x)$, $u^0(x) = \sin\left(\pi x - \frac{\sin(\pi x)}{\pi}\right)$ and $u^0(x) = \sin^4(\pi x)$.

In Tables 4.1, the L_1 and L_∞ errors and numerical orders of accuracy are given for the weighted compact schemes of different order for the first initial condition at $t = 1$. This is an easy test case and the designed order of accuracy is achieved in all cases.

For the second initial condition, used in [16], there are two critical points where $f' = 0$ but $f''' \neq 0$. Table 4.2 contains the errors and numerical orders of accuracy at $t = 2$. We can observe, in the L_1 norm, all the weighted compact schemes can achieve the designed order of accuracy. However, in the L_∞ norm, the order of accuracy achieved seems to be lower than the designed order. We will discuss this issue further in the next subsection.

The third case is a more demanding test case because it has a higher order critical point with $f' = f'' = f''' = 0$ at $x = 0$. Table 4.3 contains the numerical results at $t = 10$. We observe that all the schemes reach the designed accuracy much later during the mesh refinement than that for the previous two initial conditions.

4.2. The influence of ε and the mapped function for the smoothness indicator

The parameter ε in (2.13) has some effect on the accuracy of WENO schemes for smooth solutions [16]. In order to test the role of this parameter on the rate of convergence of the weighted compact schemes, we simulate the linear equation (4.1) with the initial condition $u^0(x) = \sin\left(\pi x - \frac{\sin(\pi x)}{\pi}\right)$, which is the one most sensitive to the choice of ε for regular WENO schemes [16]. In Table 4.4, we list the errors and numerical orders of accuracy for the fifth order weighted compact scheme using $\varepsilon = 10^{-6}$ and $\varepsilon = 10^{-20}$. It can be observed that

Table 4.1
L_1 and L_∞ errors and numerical orders of accuracy on $u_t + u_x = 0$ with $u_0(x) = \sin(\pi x)$ for the fourth order, sixth order and eighth order weighted compact schemes

Method	N	L_1 error	L_1 order	L_∞ error	L_∞ order
WCOMP4	10	1.68E−2		2.73E−2	
	20	8.16E−4	4.36	1.46E−3	4.22
	40	3.35E−5	4.61	5.83E−5	4.65
	80	1.56E−6	4.43	2.66E−6	4.45
	160	8.10E−8	4.28	1.34E−7	4.31
WCOMP6	10	2.45E−3		5.38E−3	
	20	3.31E−5	6.21	1.01E−4	5.74
	40	4.60E−7	6.18	2.44E−6	5.37
	80	6.93E−9	6.05	6.60E−8	5.21
	160	9.30E−11	6.22	1.61E−9	5.36
WCOMP8	10	2.52E−4		4.51E−4	
	20	3.23E−7	9.61	7.41E−7	9.25
	40	5.46E−10	9.21	1.48E−9	8.97
	80	1.16E−12	8.88	3.19E−12	8.86
	160	2.96E−15	8.61	6.79E−15	8.88

N is the total number of grid points in a uniform mesh. $t = 1$.

Table 4.2
L_1 and L_∞ errors and numerical orders of accuracy on $u_t + u_x = 0$ with $u_0(x) = \sin(\pi x - \sin(\pi x)/\pi)$ for the fourth order, sixth order and eight order weighted compact schemes

Method	N	L_1 error	L_1 order	L_∞ error	L_∞ order
WCOMP4	10	5.80E−2		1.29E−1	
	20	4.99E−3	3.54	1.09E−2	3.57
	40	3.40E−4	3.88	9.68E−4	3.49
	80	1.73E−5	4.30	7.95E−5	3.61
	160	8.81E−7	4.29	7.16E−6	3.47
WCOMP6	10	2.43E−2		5.98E−2	
	20	6.16E−4	5.31	1.86E−3	5.01
	40	6.53E−6	6.56	3.05E−5	5.93
	80	5.47E−8	6.90	4.79E−7	5.99
	160	5.10E−10	6.74	8.16E−9	5.88
WCOMP8	10	1.24E−2		3.11E−2	
	20	6.48E−5	7.58	1.55E−4	7.65
	40	2.23E−7	8.18	8.46E−7	7.52
	80	8.17E−10	8.09	6.33E−9	7.06
	160	2.66E−12	8.26	3.92E−11	7.34

N is the total number of grid points in a uniform mesh. $t = 2$.

Table 4.3
L_1 and L_∞ errors and numerical orders of accuracy on $u_t + u_x = 0$ with $u_0(x) = \sin^4(\pi x)$ for the fourth order, sixth order and eighth order weighted compact schemes

Method	N	L_1 error	L_1 order	L_∞ error	L_∞ order
WCOMP4	10	3.56E−1		4.46E−1	
	20	1.42E−1	1.33	3.12E−1	0.52
	40	2.62E−2	2.44	6.18E−2	2.33
	80	2.21E−3	3.57	4.20E−3	3.88
	160	1.64E−4	3.76	6.20E−4	2.76
WCOMP6	10	3.56E−1		4.68E−1	
	20	9.27E−2	1.94	2.07E−1	1.18
	40	7.22E−3	3.68	1.40E−2	3.88
	80	3.06E−4	4.56	1.17E−3	3.59
	160	1.10E−6	8.12	5.15E−6	7.82
WCOMP8	10	2.78E−1		4.04E−1	
	20	5.56E−2	2.32	1.07E−1	1.91
	40	5.16E−4	6.75	1.67E−3	6.00
	80	1.87E−6	8.10	7.46E−6	7.81
	160	3.05E−9	9.26	2.07E−8	8.49

N is the total number of grid points in a uniform mesh. $t = 10$.

there is essentially no difference between the results with these two different values of ε. Similar conclusions hold for the weighted compact schemes of other orders of accuracy. It seems that the convergence rate of the weighted compact schemes is less sensitive to the choice of ε than the regular WENO schemes [16].

For the regular fifth order WENO scheme, Henrich et al. [16] pointed out that the nonlinear weights with the smoothness indicator in [19] may lose accuracy at certain smooth extrema. To solve this problem, they introduced a mapping function:

$$g_k^r(\omega) = \frac{\omega(C_k^r + (C_k^r)^2 - 3C_k^r\omega + \omega^2)}{(C_k^r)^2 + (1 - 2C_k^r)\omega}, \tag{4.2}$$

where $\omega \in [0, 1]$ and $r = 0, 1, 2$. This function is monotonically increasing with a finite slope and $g_k^r(0) = 0$, $g_k^r(1) = 1$, $g_k^r(C_k^r) = C_k^r$, $(g_k^r(C_k^r))' = 0$ and $(g_k^r(C_k^r))'' = 0$. The mapped nonlinear weights are given by

Table 4.4
The comparison between the results of different ε for L_1 and L_∞ errors and numerical orders of accuracy on $u_t + u_x = 0$ with $u_0(x) = \sin(\pi x - \sin(\pi x)/\pi)$

ε	N	L_1 error	L_1 order	L_∞ error	L_∞ order
10^{-6}	10	5.92E−2		1.30E−1	
	20	4.43E−3	3.74	1.17E−2	3.48
	40	2.85E−4	3.96	9.65E−4	3.60
	80	1.51E−5	4.23	9.52E−5	3.34
	160	7.46E−7	4.34	9.11E−6	3.38
10^{-20}	10	5.92E−2		1.30E−1	
	20	4.43E−3	3.74	1.17E−2	3.48
	40	2.85E−4	3.96	9.65E−4	3.60
	80	1.52E−5	4.23	9.56E−5	3.34
	160	7.72E−7	4.30	9.59E−6	3.32

Fifth order weighted compact scheme. N is the total number of grid points in a uniform mesh. $t = 2$.

$$\omega_k^{rM} = g_k^r(\omega_k^r). \tag{4.3}$$

The WENO schemes based on these mapped nonlinear weights are able to achieve the designed high order accuracy for general smooth solutions independent of the choice of ε [16]. We test these mapped nonlinear weights, with $\varepsilon = 10^{-20}$, for our weighted compact schemes. The results are listed in Table 4.5. Compared with the results in Table 4.2, we observe an apparent improvement for the order of accuracy in the L_∞ norm, and also the magnitude of the errors for the same mesh has been significantly reduced for most cases. Similar conclusions hold for higher order weighted compact schemes.

Table 4.5
L_1 and L_∞ errors and numerical orders of accuracy on $u_t + u_x = 0$ with $u_0(x) = \sin(\pi x - \sin(\pi x)/\pi)$ for the mapped weighted compact scheme with $\varepsilon = 10^{-20}$

Method	N	L_1 error	L_1 order	L_∞ error	L_∞ order
MWCOMP4	10	3.89E−2		9.14E−2	
	20	2.56E−3	3.93	6.56E−3	3.80
	40	1.33E−4	4.27	3.64E−4	4.17
	80	6.95E−6	4.26	1.87E−5	4.28
	160	3.91E−7	4.15	1.04E−6	4.17
MWCOMP5	10	3.42E−2		7.59E−2	
	20	1.48E−3	4.53	3.99E−3	4.25
	40	5.35E−5	4.79	1.63E−4	4.62
	80	1.73E−6	4.95	4.88E−6	5.06
	160	5.47E−8	4.99	1.54E−7	4.99
MWCOMP6	10	1.53E−2		3.64E−2	
	20	2.22E−4	6.10	6.68E−4	5.77
	40	1.98E−6	6.80	6.36E−6	6.71
	80	1.72E−8	6.85	5.81E−8	6.77
	160	1.62E−10	6.73	5.61E−10	6.69
MWCOMP8	10	7.25E−3		1.64E−2	
	20	4.19E−5	7.43	1.24E−4	7.04
	40	9.89E−8	8.73	3.25E−7	8.58
	80	2.06E−10	8.91	6.84E−10	8.89
	160	2.02E−11	3.35	4.21E−11	4.02

N is the total number of grid points in a uniform mesh. $t = 2$.

5. Numerical tests and comparison

5.1. Scalar cases

The first example is the following nonlinear scalar Burgers' equation

$$u_t + \left(\frac{u^2}{2}\right)_x = 0 \tag{5.1}$$

with the initial condition $u(x,0) = 0.5 + \sin(\pi x)$. In Fig. 5.1, we show the solution at $t = 1.5/\pi$ with a shock near $x = 1.2$. We can observe that all the weighted compact schemes give similarly good results for this scalar problem. They perform very well to capture this discontinuity.

Our second scalar example is the Buckley–Leverett problem that is governed by the equation

$$u_t + \left(\frac{4u^2}{4u^2 + (1-u)^2}\right)_x = 0. \tag{5.2}$$

The initial condition is $u = 1$ for $-\frac{1}{2} \leqslant x \leqslant 0$ and $u = 0$ elsewhere. The solution is computed up to $t = 0.4$. Fig. 5.2 shows the numerical solutions of the fourth, sixth and eighth order weighted compact schemes. Again, all these schemes perform similarly well for this example.

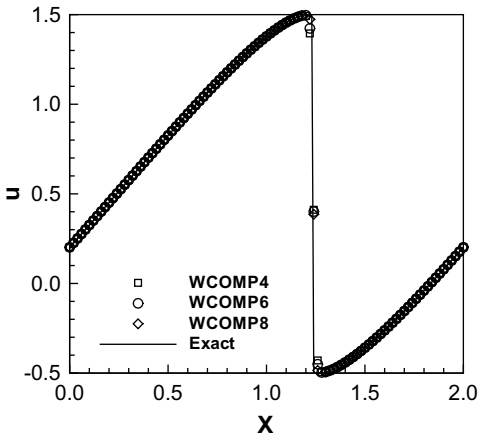

Fig. 5.1. Solution of the nonlinear Burgers' equation with the initial condition $u(x,0) = 0.5 + \sin(\pi x)$ at $t = 1.5/\pi$ with 100 grid points.

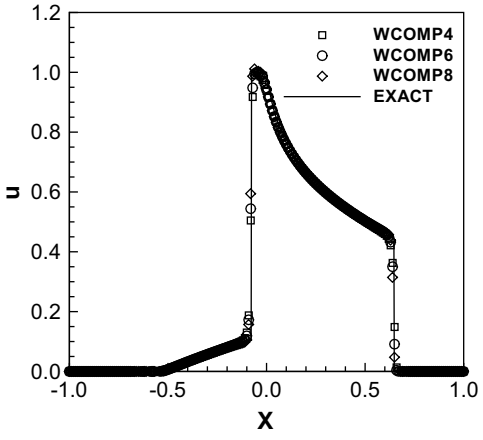

Fig. 5.2. Solution of the Buckley–Leverett problem. $t = 0.4$. $N = 200$ grid points.

5.2. 1D Euler equation

The 1D Euler equation is given by

$$U_t + F(U)_x = 0, \tag{5.3}$$

where $U = (\rho, \rho u, e)^{\mathrm{T}}$, $F(U) = (\rho u, \rho u^2 + p, u(e+p))^{\mathrm{T}}$. Here ρ is the density, u is the velocity, e is the total energy, p is the pressure which is related to the total energy by $e = \frac{p}{\gamma-1} + \frac{1}{2}\rho u^2$, the ratio of specific heat $\gamma = 1.4$.

We consider three typical examples. The first problem is the Shu–Osher problem [39]. It describes the interaction of a Mach 3 shock with a density wave. A Mach 3 shock is initially located at $x = -4$ and moves to the right. A sine wave is superposed to the density in the right region to the shock which is given by $(\rho, v, P) = (1 + \varepsilon \sin(5x), 0, 1)$. The amplitude of the sine wave is $\varepsilon = 0.2$. The value downstream of the shock wave is computed by the Rankine–Hugoniot relation [34].

The second is the Sod problem [41]. The initial condition is:

$$(\rho_{\mathrm{L}}, q_{\mathrm{L}}, p_{\mathrm{L}}) = (1, 0, 1) \quad \text{when } x < 0,$$
$$(\rho_{\mathrm{R}}, q_{\mathrm{R}}, p_{\mathrm{R}}) = (0.125, 0, 0.1) \quad \text{when } x > 0.$$

The third is the Lax problem [24] with the initial condition:

$$(\rho_{\mathrm{L}}, q_{\mathrm{L}}, p_{\mathrm{L}}) = (0.445, 0.698, 3.528) \quad \text{when } x < 0,$$
$$(\rho_{\mathrm{R}}, q_{\mathrm{R}}, p_{\mathrm{R}}) = (0.5, 0, 0.571) \quad \text{when } x > 0.$$

Figs. 5.3–5.5 show the density distributions of the numerical solutions corresponding to the three problems described above. We observe a good non-oscillatory resolution of the discontinuities by all the compact schemes, which is comparable to the resolution of discontinuities by regular WENO schemes [19]. The resolution to the smooth solution structure in Fig. 5.3 is very good, especially for the higher order weighted compact schemes.

5.3. 2D Euler equation

The 2D Euler equation is given by

$$U_t + F(U)_x + G(U)_y = 0, \tag{5.4}$$

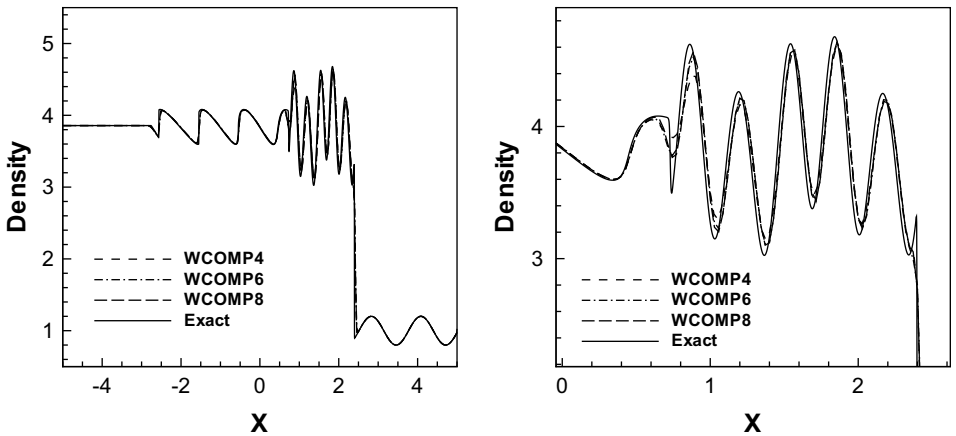

(a) global view (b) locally zoomed

Fig. 5.3. Density distribution for the Shu–Osher problem with 400 grid points at $t = 1.8$. The "exact solution" is obtained by WENO5 with 8000 grid points.

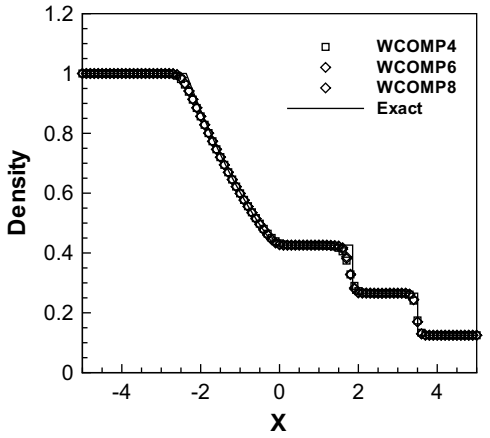

Fig. 5.4. Density distribution for the Sod problem with 100 grid points at $t = 2$.

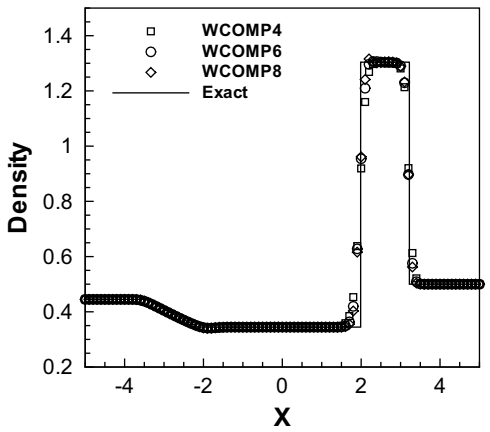

Fig. 5.5. Density distribution for the Lax problem with 100 grid points at $t = 1.3$.

where $U = (\rho, \rho u, \rho v, e)^{\mathrm{T}}$, $F(U) = (\rho u, \rho u^2 + p, \rho uv, u(e + p))^{\mathrm{T}}$, $G(U) = (\rho v, \rho uv, \rho v^2 + p, v(e + p))^{\mathrm{T}}$. Here ρ is the density, u is the velocity component in the x direction, v is the velocity component in the y direction, e is the total energy, p is the pressure which is related to the total energy by $e = \frac{p}{\gamma-1} + \frac{1}{2}\rho u^2$, the ratio of specific heat $\gamma = 1.4$.

For the two dimensional Euler equation, we solve three problems. The first example is the double Mach reflection problem. This example is well studied using high order WENO schemes in, e.g. [19,47]. It contains strong shock waves and contact discontinuity which is a good example to test the numerical scheme to show the ability to capture strong shock wave and the resolution for small scale structure. The computational domain for this problem is $[0, 4] \times [0, 1]$. The reflecting wall lies at the bottom, starting from $x = \frac{1}{6}$. Initially, a right moving Mach 10 shock wave is positioned at $x = \frac{1}{6}$, $y = 0$. It has an angle 60° with the x axis. The boundary condition is the same as that in [19]. The grid is uniform with $\frac{1}{\Delta x} = \frac{1}{\Delta y} = \frac{1}{480}$. Fig. 5.6 shows the density contours obtained by the fifth order WENO scheme and the weighted compact schemes. The contours zoomed around the contact discontinuity and Mach stem region are given in Fig. 5.7. We can clearly see that the weighted compact scheme has almost the same ability to capture strong shock waves as the regular WENO scheme [19] while the resolution of the small scale waves is improved.

The second example is the Rayleigh–Taylor instability. It happens on an interface between fluids with different densities when an acceleration is directed from the heavy fluid to the light one. The instability has a fingering nature, with bubbles of light fluid rising into the ambient heavy fluid and spikes of heavy falling into

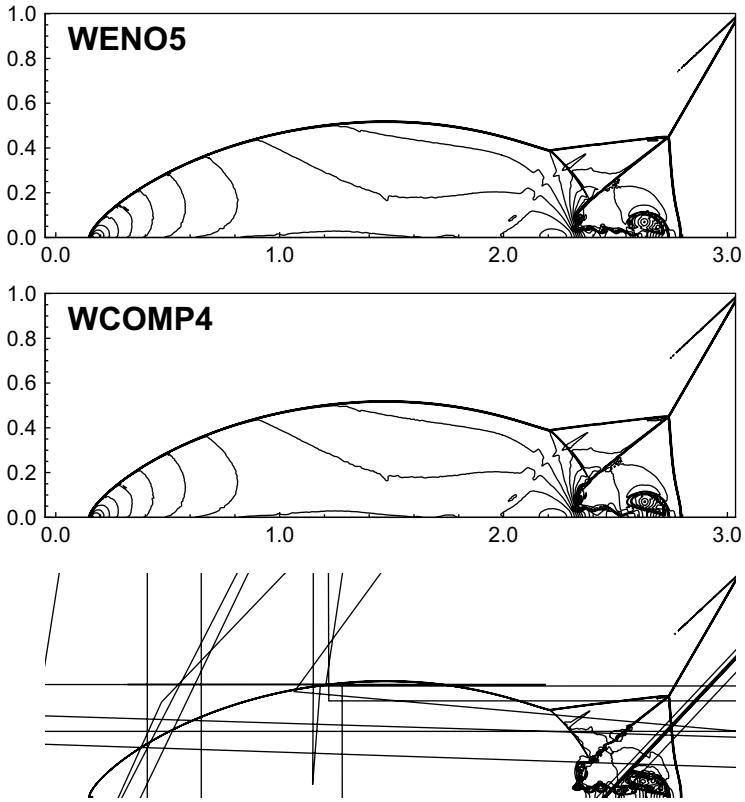

the light fluid. This problem has been extensively studied using high order shock capturing schemes in the literature, see, e.g. [47]. Previous studies show that there are many small scale structures. It is a good example to test the resolution of the numerical schemes. Following the simulation of Zhang et al. [47], the computational domain is $[0, \frac{1}{4}] \times [0, 1]$; the initial interface is at $y = \frac{1}{2}$. The heavy fluid with $\rho = 2$ is below in the interface and the light fluid with density $\rho = 1$ is above the interface. The pressure is continuous across the interface. A small perturbation is given to the velocity component in y direction. Thus, for $0 \leqslant y < \frac{1}{2}$, $\rho = 2$, $u = 0$, $p = 2y + 1$, $v = -0.025c\cos(8\pi x)$; and for $\frac{1}{2} \leqslant y \leqslant 1$, $\rho = 1$, $u = 0$, $p = y + \frac{3}{2}$, $v = -0.025c\cos(8\pi x)$. Here, $c = \sqrt{\gamma p/\rho}$ is the sound speed. The ratio of specific heats $\gamma = \frac{5}{3}$. A source term ρ is added to the right hand side of the third equation and ρv is added to the fourth equation of the Euler system (5.4). The simulation time is $t = 1.95$. Fig. 5.8 shows the density contours of the numerical results obtained by the fourth order, sixth order and eighth order weighted compact schemes. For comparison, we also show the numerical result obtained by the fifth order WENO scheme [19]. We can observe that the weighted compact schemes can produce more small vortices in the shear layer, indicating that they have better resolution to capture small scale structures.

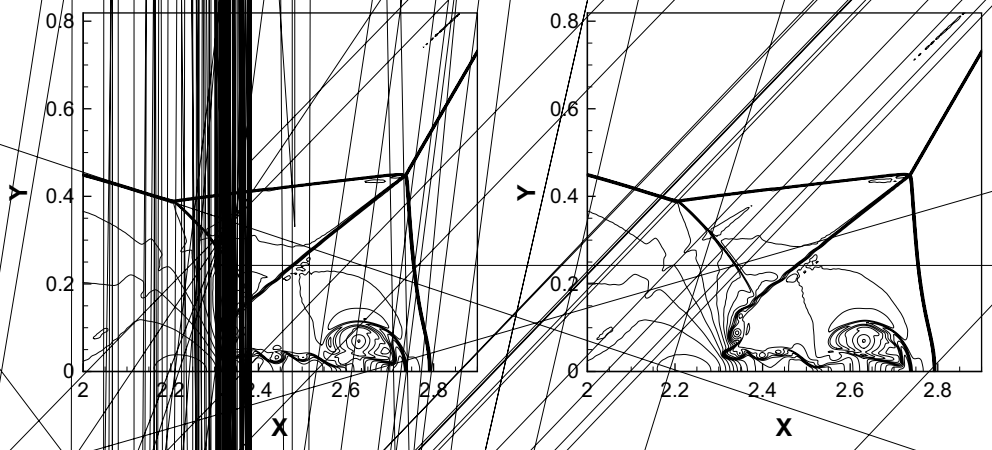

(a) WENO5 (b) WCOMP4

Our third example is a shock vortex interaction problem. It contains very important aerodynamic and aeroacoustic phenomena. As the shock interacts with the vortex, the shock and vortex are deformed. At the same time, there are three sound waves generated. This problem is extensively studied in literature [12–14,18,45,46]. The problem is set up as follows: the computational domain is $[-20,20]\times[-20,20]$. An $M_s = 1.2$ shock wave is set up to be stationary at $x = 0$. An isentropic vortex of $M_v = 0.25$ is initially superposed in the position $(4,0)$ which moves toward the shock wave at the speed of shock. The initial value of the vortex parameters is set up as follows [18,45]: tangential velocity, $u_\theta = M_v r e^{\frac{1-r^2}{2}}$; radial velocity, $u_r = 0$; pressure, $p(r) = \frac{1}{\gamma}(1-\frac{\gamma-1}{2}M_v^2 e^{(1-r^2)})^{\frac{\gamma}{\gamma-1}}$; density, $\rho(r) = (1-\frac{\gamma-1}{2}M_v^2 e^{(1-r^2)})^{\frac{1}{\gamma-1}}$. Fig. 5.9 contains the density contours at two typical times $t = 3$ and $t = 8$. At $t = 3$, the shock wave is just passing through the vortex. It is deformed into S shape. The reflected shock wave is a Mach reflection at $t = 8$. The first sound has the quadrupolar nature which is the same with that in the literature [18,45]. We note that there are some noises (wriggles in the contours) for the sixth and eighth order weighted compact schemes at the later time $t = 8$ in Fig. 5.9. However, the magnitude of these wriggles is very small.

6. Convergence to steady state solutions of the Euler equations

Convergence to steady state solutions for Euler equations or in general for hyperbolic systems with shocks is a problem for weighted type schemes [44]. Often the numerical residue does not converge to machine zero

ation error. There is a debate on the impl f driving the residue to
ffected when the residue settles at the level uncation error, however
he numerical residue could reach close to m zero for steady state cal-
he convergence to steady state solution o quations for the fourth

he weighted compact schemes with a 2D e ortex [36]. It is a smooth
on without any discontinuities. The com al domain is set to be
ake a 400×400 equally spaced mesh m the simulation until

rizontal line $y = 0$ and the evolution of t ged residue and for the
t can be seen that the averaged residue of th order weighted com-
r this smooth problem, a little higher tha r the regular fifth order
r practical considerations.

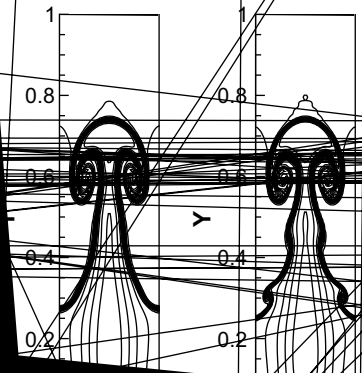

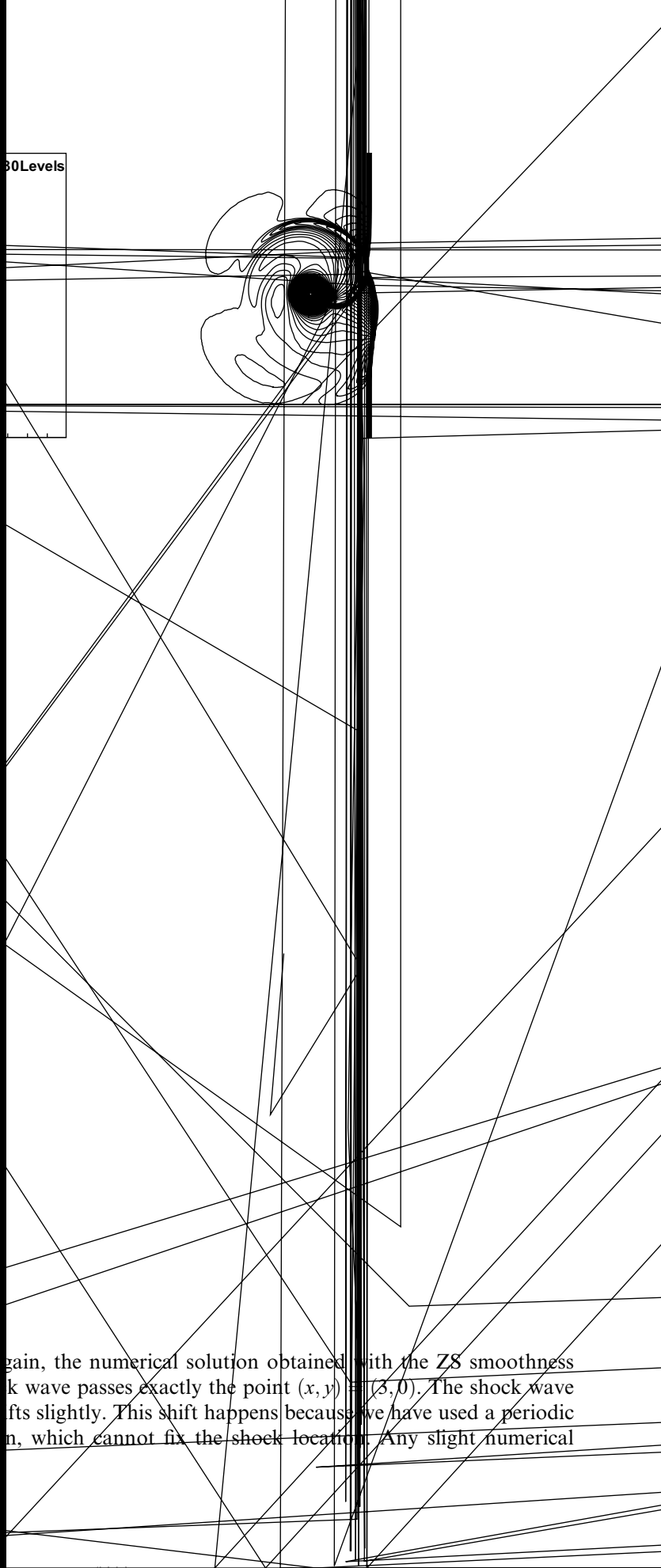

gain, the numerical solution obtained with the ZS smoothness
k wave passes exactly the point $(x, y) = (3, 0)$. The shock wave
fts slightly. This shift happens because we have used a periodic
n, which cannot fix the shock location. Any slight numerical

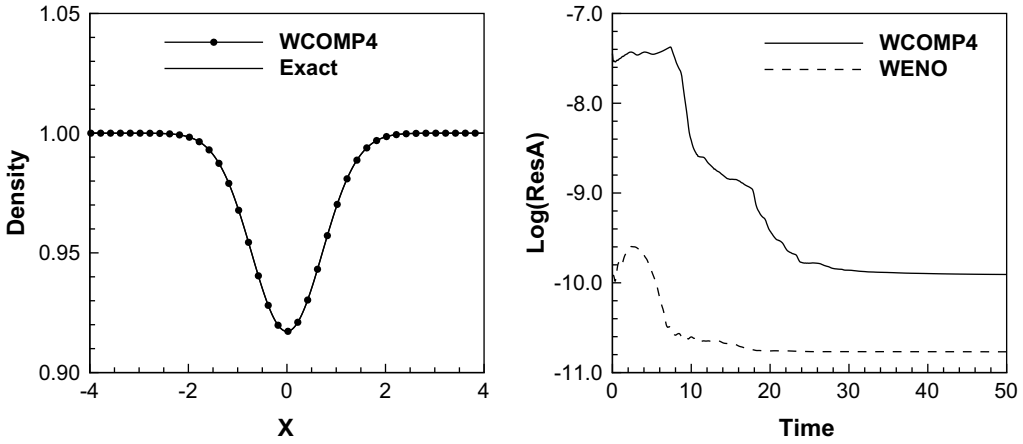

Fig. 6.10. Density distribution (left) and the evolution of the averaged residue (right) for the two dimensional isentropic vortex.

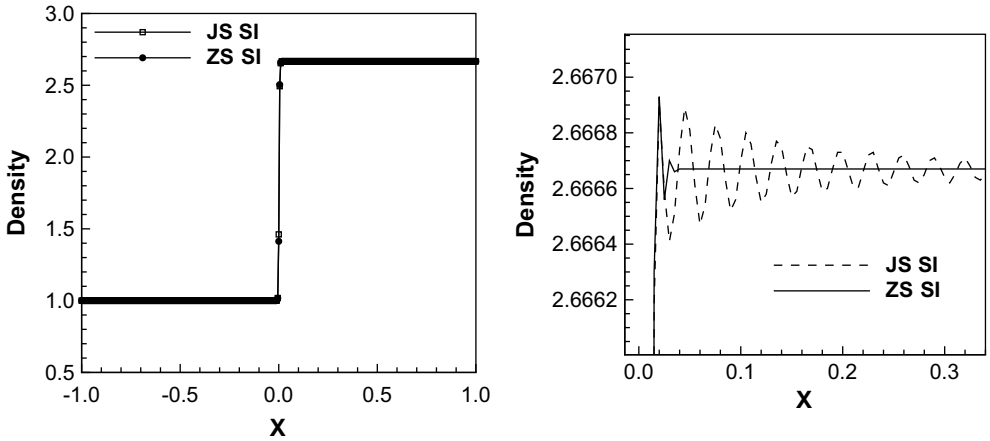

Fig. 6.11. The density distribution for the one dimensional steady shock with $M_\infty = 2$. (Left) The global view; (right) locally zoomed.

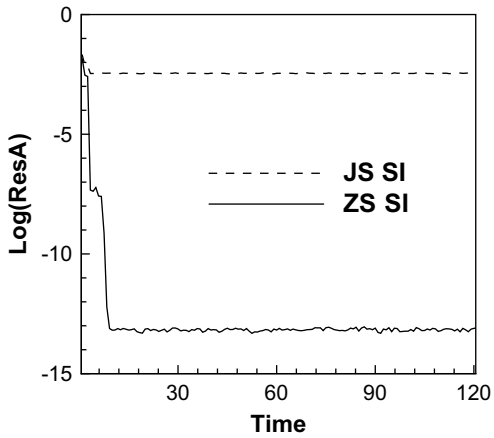

Fig. 6.12. The evolution of the averaged residue of fourth order weighted compact scheme for the one dimensional steady shock with $M_\infty = 2$.

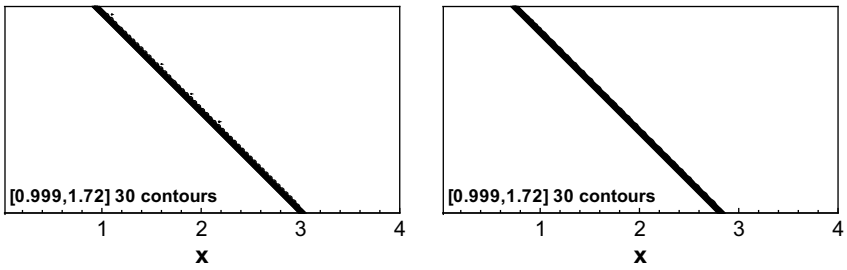

Fig. 6.13. Density contours of an 45° oblique shock with $M_\infty = 2$ with the fourth order weighted compact scheme. (left) With the ZS smoothness indicator; (right) with the JS smoothness indicator.

perturbation may shift the shock. Fig. 6.14 shows the evolution of the averaged residue. The convergence ability of the ZS smoothness indicator is much better.

7. Concluding remarks

We have modified and extended the weighted compact schemes proposed by Deng and Zhang [9] to design a class of weighted compact schemes with increasingly higher order of accuracy. The weighted compact scheme in [9] was proposed based on the idea of the WENO scheme [19] and the cell-centered compact scheme [26], which has better short wave resolution than other compact schemes. The cell centered values can be obtained exactly in a staggered grid or interpolated in a regular grid. The weighted compact scheme is a result of the cell-centered compact scheme coupled with a nonlinear weighted interpolation for the cell centered values of the flux.

Instead of interpolating the conservative variables as in [9], we obtain the cell centered flux directly with high order (up to eighth order) accuracy from a WENO interpolation. Through using the Lax–Friedrichs flux splitting and characteristic-wise projection, the resulted weighted interpolation formulae have the same structure as those of a regular WENO scheme. Therefore, the analysis and even many pieces of the code can be copied from that of the regular WENO schemes. Through a systematic analysis, tests and comparison, we conclude that the weighted compact schemes discussed in this paper have the same ability to capture strong discontinuities as the regular WENO schemes, while the resolution of short frequency waves in the solution is improved.

The convergence to steady state solutions of Euler equations is studied for the fourth order weighted compact scheme. Even though the interpolation is different from the reconstruction for the regular WENO

scheme, the weighted compact scheme and the regular WENO scheme have the same smoothness indicator. In addition, we test two different kinds of smoothness indicators. One is the original smooth indicator proposed by Jiang and Shu [19], the other is the smooth indicator proposed by Zhang and Shu [44]. It is found that the ZS smoothness indicator is more suitable to simulate steady state solutions of the Euler equations including strong shock waves, similar to the situation for regular WENO schemes [44]. The slight post-shock oscillation is removed or reduced and convergence toward steady state is improved significantly.

References

[1] N.A. Adams, K. Shariff, A high-resolution hybrid compact-ENO scheme for shock–turbulence interaction problems, J. Comput. Phys. 127 (1996) 27–51.
[2] D.S. Balsara, C.-W. Shu, Monotonicity preserving weighted essentially non-oscillatory schemes with increasingly high order of accuracy, J. Comput. Phys. 160 (2000) 405–452.
[3] B.J. Boersma, A staggered compact finite difference formulation for the compressible Navier–Stokes equations, J. Comput. Phys. 208 (2005) 675–690.
[4] C. Canuto, M.Y. Hussaini, A. Quarteroni, T.A. Zang, Spectral Methods in Fluid Dynamics, Springer-Verlag, New York, 1987.
[5] M.H. Carpenter, D. Gottlieb, S. Abarbanel, The stability of numerical boundary treatments for compact high-order finite-difference schemes, J. Comput. Phys. 108 (1993) 272–295.
[6] B. Cockburn, C.-W. Shu, Nonlinearly stable compact schemes for shock calculations, SIAM J. Numer. Anal. 31 (1994) 607–627.
[7] G.S. Constantinescu, S.K. Lele, Large eddy simulation of a near sonic turbulent jet and its radiated noise, AIAA Paper, 2001, 2001-0376.
[8] X. Deng, H. Maekawa, Compact high-order accurate nonlinear schemes, J. Comput. Phys. 130 (1997) 77–91.
[9] X. Deng, H. Zhang, Developing high-order weighted compact nonlinear schemes, J. Comput. Phys. 165 (2000) 22–44.
[10] D. Fu, Y. Ma, L. Hong, Upwind compact schemes and applications, Proceedings of the Fifth Symp. on Comput. Fluid Dyn., vol. 1, Japan Soc. of Comput. Fluid Dyn., 1993.
[11] D. Gottlieb, S.A. Orszag, Numerical Analysis of Spectral Methods, SIAM, Philadelphia, 1977.
[12] F. Grasso, S. Pirozzoli, Shock wave–thermal inhomogeneity interactions: analysis and numerical simulations of sound generation, Phys. Fluids 12 (2000) 205–219.
[13] F. Grasso, S. Pirozzoli, Shock-wave–vortex interactions: shock and vortex deformations, and sound production, Theor. Comput. Fluid Dyn. 13 (2000) 421–456.
[14] F. Grasso, S. Pirozzoli, Simulations and analysis of the coupling process of compressible vortex pairs: free evolution and shock induced coupling, Phys. Fluids 13 (2001) 1343–1366.
[15] A. Harten, B. Engquist, S. Osher, S. Chakravarthy, Uniformly high order essentially non-oscillatory schemes, III, J. Comput. Phys. 71 (1987) 231–303.
[16] A.K. Henrick, T.D. Aslam, J.M. Powers, Mapped weighted essentially non-oscillatory schemes: achieving optimal order near critical points, J. Comput. Phys. 207 (2005) 542–567.
[17] R.S. Hirsh, High order accurate difference solutions of fluid mechanics problems by a compact differencing technique, J. Comput. Phys. 19 (1975) 90–109.
[18] O. Inoue, Y. Hattori, Sound generation by shock–vortex interactions, J. Fluid Mech. 380 (1999) 81–116.
[19] G.-S. Jiang, C.-W. Shu, Efficient implementation of weighted ENO schemes, J. Comput. Phys. 126 (1996) 202–228.
[20] G.-S. Jiang, C.-C. Wu, A high-order WENO finite difference scheme for the equations of ideal magnetohydrodynamics, J. Comput. Phys. 150 (1999) 561–594.
[21] L. Jiang, H. Shan, C.Q. Liu, Weighted compact scheme, Int. J. Comput. Fluid Dyn. 15 (2001) 147–155.
[22] J. Kim, P. Moin, R. Moser, Turbulence statistics in fully developed channel flow at low Reynolds number, J. Fluid Mech. 177 (1987) 133–166.
[23] H.-O. Kreiss, S.A. Orszag, M. Israeli, Numerical simulation of viscous incompressible flow, Annu. Rev. Fluid Mech. 6 (1974) 281–318.
[24] P.D. Lax, Commun. Pure Appl. Math. 7 (1954) 159.
[25] S.S. Lee, S.K. Lele, P. Moin, Interaction of isotropic turbulence with shock waves: effect of shock strength, J. Fluid Mech. 340 (1997) 225.
[26] S.K. Lele, Compact finite difference schemes with spectral-like resolution, J. Comput. Phys. 103 (1992) 16–42.
[27] X.-D. Liu, S. Osher, T. Chan, Weighted essentially non-oscillatory schemes, J. Comput. Phys. 115 (1994) 200–212.
[28] K. Mahesh, A family of high order finite difference schemes with good spectral resolution, J. Comput. Phys. 145 (1998) 332–358.
[29] K. Mahesh, S.K. Lele, P. Moin, The influence of entropy fluctuations on the interaction of turbulence with a shock wave, J. Fluid Mech. 334 (1997) 353–379.
[30] P. Moin, K. Squires, W. Cabot, S. Lee, A dynamic subgrid-scale model for compressible turbulence and scalar transport, Phys. Fluids A 3 (1991) 2746.
[31] S. Nagarajan, S.K. Lele, J.H. Ferziger, A robust high-order compact method for large eddy simulation, J. Comput. Phys. 191 (2003) 392–419.
[32] S. Pirozzoli, Conservative hybrid compact-WENO schemes for shock–turbulence interaction, J. Comput. Phys. 178 (2002) 81–117.

[33] D. Ponziani, S. Pirozzoli, F. Grasso, Development of optimized weighted-ENO schemes for multiscale compressible flows, Int. J. Numer. Methods Fluids 42 (2003) 953–977.
[34] M.A. Saad, Compressible Fluid Flow, Prentice-Hall, 1993.
[35] K. Sebastian, C.-W. Shu, Multi domain WENO finite difference method with interpolation at sub-domain interfaces, J. Sci. Comput. 19 (2003) 405–438.
[36] B. Cockburn, C. Johnson, C.-W. Shu, E. Tadmor, Essentially non-oscillatory and weighted essentially non-oscillatory schemes for hyperbolic conservation laws, Advanced Numerical Approximation of Nonlinear Hyperbolic Equations, in: A. Quarteroni (Ed.), Lecture Notes in Mathematics, vol. 1697, Springer, 1998, pp. 325–432.
[37] C.-W. Shu, High order weighted essentially non-oscillatory schemes for convection dominated problems, SIAM Rev. (in press).
[38] C.-W. Shu, S. Osher, Efficient implementation of essentially non-oscillatory shock capturing schemes, J. Comput. Phys. 77 (1988) 439–471.
[39] C.-W. Shu, S. Osher, Efficient implementation of essentially non-oscillatory shock capturing schemes II, J. Comput. Phys. 83 (1989) 32–78.
[40] R.K. Shukla, X. Zhong, Derivation of high-order compact finite difference schemes for non-uniform grid using polynomial interpolation, J. Comput. Phys. 204 (2005) 404–429.
[41] G.A. Sod, A survey of several finite difference methods for systems of nonlinear hyperbolic conservation laws, J. Comput. Phys. 27 (1978) 1–31.
[42] C.K.W. Tam, J.C. Webb, Dispersion-relation-preserving finite difference schemes for computational acoustics, J. Comput. Phys. 107 (1993) 262–281.
[43] Z.J. Wang, R.F. Chen, Optimized weighted essentially non-oscillatory schemes for linear waves with discontinuity, J. Comput. Phys. 174 (2001) 381–404.
[44] S. Zhang, C.-W. Shu, A new smoothness indicator for WENO schemes and its effect on the convergence to steady state solutions, J. Sci. Comput. 31 (2007) 273–305.
[45] S. Zhang, Y.-T. Zhang, C.-W. Shu, Multistage interaction of a shock wave and a strong vortex, Phys. Fluid 17 (2005) 116101.
[46] S. Zhang, Y.-T. Zhang, C.-W. Shu, Interaction of an oblique shock wave with a pair of parallel vortices: shock dynamics and mechanism of sound generation, Phys. Fluids 18 (2006) 126101.
[47] Y.-T. Zhang, J. Shi, C.-W. Shu, Y. Zhou, Numerical viscosity and resolution of high-order weighted essentially nonoscillatory schemes for compressible flows with high Reynolds numbers, Phys. Rev. E 68 (2003) 046709.
[48] X. Zhong, High-order finite-difference schemes for numerical simulation of hypersonic boundary-layer transition, J. Comput. Phys. 144 (1998) 662–709.